New Insights From Conceptual Design of an Additive Manufactured 300 W Microgas Turbine Toward Unmanned Aerial Vehicle Applications

Lukas Badum
Turbomachinery and Heat Transfer Laboratory,
Aerospace Engineering Department,
Technion—Israel Institute of Technology,
Technion City 3200003, Haifa, Israel
e-mail: lukas@campus.technion.ac.il

Boris Leizeronok
Turbomachinery and Heat Transfer Laboratory,
Aerospace Engineering Department,
Technion—Israel Institute of Technology,
Technion City 3200003, Haifa, Israel
e-mail: borisl@technion.ac.il

Beni Cukurel
Turbomachinery and Heat Transfer Laboratory,
Aerospace Engineering Department,
Technion—Israel Institute of Technology,
Technion City 3200003, Haifa, Israel
e-mail: beni@cukurel.org

Owing to the high energy density of hydrocarbon fuels, ultramicrogas turbines (UMGT) with power outputs below 1 kW have clear potential as battery replacement in drones. However, previous works on gas turbines of this scale revealed severe challenges due to air bearing failures, heat transfer from turbine to compressor, rotordynamic instability, and manufacturing limitations. To overcome these obstacles, a novel gas turbine architecture is proposed based on conventional roller bearing technology that operates at up to 500,000 RPM and an additively manufactured monolithic rotor in cantilevered configuration, equipped with internal cooling blades. The optimum turbomachinery design is elaborated using diabatic cycle calculation, coupled with turbomachinery meanline design code. This approach provides new insights on the interdependencies of heat transfer, component efficiency, and system electric efficiency. Thereby, a reduced design pressure ratio of 2.5 with 1200 K turbine inlet temperature (TIT) is identified as most suitable for 300 W electric power output. In following, a review of available additive manufacturing technologies yields material properties, surface roughness, and design constraints for the monolithic rotor. Rotordynamic simulations are then conducted for four available materials using a simplified rotor model to identify valid permanent magnet dimensions that would avoid operation close to bending modes. To complete the baseline engine architecture, a novel radial inflow combustor concept is proposed based on porous inert media combustion. computational fluid dynamics (CFD) simulations are conducted to quantify compressor efficiency and conjugate heat transfer (CHT) analysis of the monolithic rotor is performed to assess the benefit of the internal cooling cavity and vanes for different rotor materials. It is demonstrated that the cavity flow absorbs large amount of heat flux from turbine to compressor, thus cooling the rotor structure and improving the diabatic cycle efficiency. Finally, the results of this conceptual study show that ultramicrogas turbine with electric efficiency of up to 5% is feasible, while energy density is increased by factor of 3.6, compared to lithium-ion batteries. [DOI: 10.1115/1.4048695]

Keywords: ultramicro gas turbine, gas turbine architectures, additive manufacturing, ceramic materials, conjugate heat transfer analysis, rotordynamics analysis, reduced order modeling

Introduction

In civil applications, aerial drones are commonly used in entertainment, transport, and field operations, such as mapping, search and rescue, agricultural, or construction purposes [1]. The military drone market value is mainly constituted of large combat drones for high altitude long endurance and medium altitude long endurance missions [2]. However, small drones for surveillance and transport are steadily becoming an essential part of modern military technology, improving soldier safety, and enabling logistic supply of remote units. Therefore, this expanding market of small- and medium-sized unmanned aerial vehicles (UAVs) is generating a growing interest in small scale, high energy density power supply, outperforming current battery technologies. According to a recent survey, drone providers see battery life enhancement as a key growth driver for the drone market [3].

In the scope of the present effort, ultramicrogas turbines (UMGTs) with an electric power output below 1 kW are proposed as battery replacement systems due to the high energy density of hydrocarbon fuel that surpasses off-the-shelf lithium polymer batteries by up to factor of 100. UMGTs would use this energy density potential by establishing same thermodynamic cycle as large gas turbine engines, but with reduced pressure ratios, turbine inlet temperatures (TITs), and component efficiencies. Thus, despite low conversion efficiency of small-scale gas turbines, the resulting system energy density still has the potential to surpass standard lithium batteries by far, specifically addressing UAV applications with maximized flight time demands. Compared to piston engines of similar scale, UMGTs offer superior reliability, reduced noise and vibrations, and high power to weight ratio.

In order to specify an appropriate UMGT power output range, 20 drones with a takeoff weight of up to 6 kg are compared in terms of required battery power. This survey, tabulated in Appendix A and summarized in Fig. 1, indicates that a power output level in the range of 100-500 W covers the majority of UAV applications below 6 kg. However, as the drone field operation and transport applications are expected to expand, a target wattage of 300–500 W can be selected for the present microgas turbine system, resulting in a takeoff weight between 3 and 6 kg with approximate payload of 1–2.5 kg. The typical battery weight of this drone class ranges from 1 to 2.5 kg.

Manuscript received August 27, 2020; final manuscript received September 10, 2020; published online January 18, 2021. Editor: Jerzy T. Sawicki.

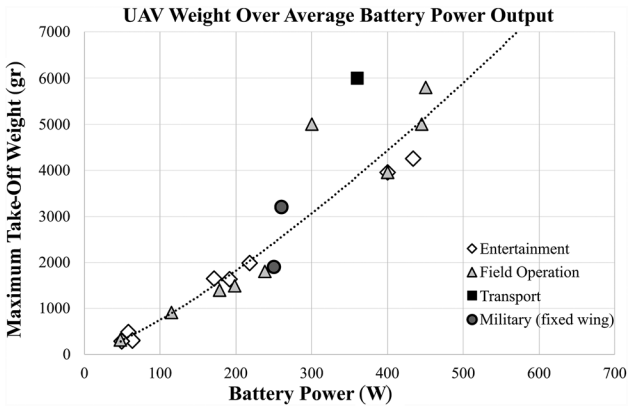

Fig. 1 UAV weight versus average battery power

Review of Previous Work

Development of UMGTs was originally initiated by an Massachusetts Institute of Technology (MIT) research group that proposed micromanufactured gas turbines based on silicon wafer material [4]. The thermodynamic target values were a TIT of up to 1600 K and a pressure ratio of above 4 [5]. However, although such high values resulted in high ideal Brayton cycle efficiency, they imposed excessive rotational speeds and unacceptable heat transfer rates from turbine to compressor. To sustain the angular velocity demand, flat air bearings with a radial gap of 15 μm were investigated in depth [6,7]. In these studies, the bearings could not provide stable operation beyond several minutes. Moreover, turbomachinery components' efficiency dropped rapidly due to low Reynolds number effects and heat flux on the compressor side [8]. Overall, these obstacles prevented successful operation on a system level.

Despite the observed difficulties, the MIT project has inspired several research groups to develop other UMGT concepts. The first self-sustained UMGT-scale Brayton cycle was demonstrated in Tohoku University. Following a feasibility analysis [9], the design pressure ratio was set to 3, with TIT of 1323 K and rotational speed of 870,000 RPM. Although target turbine and compressor diameters were 10 mm, during the project the values had to be increased to 17.4 and 16 mm, respectively [10]. Components were produced by conventional computer numerical control machining and a hydro-inertia bearing system, which relies on auxiliary air supply, was developed to sustain the high rotational speeds [11]. In order to improve rotordynamic performance, the generator was located between the compressor and the turbine, with the bearings placed on both sides of the generator. The prototype did not exceed 360,000 RPM due to whirl instability of the hydro-inertia bearings, which resulted in reduced pressure ratio, and subsequently, no electric power output was generated.

The second functioning UMGT prototype was demonstrated by a research group from Korea Institute of Machinery and Materials, who developed a recuperated gas turbine toward 500 W power output at 400,000 RPM [12–15]. Rotordynamic tests and heat transfer studies were presented in subsequent publications, however a system level engine model was not considered in the preliminary stage. The bearings were located before the generator and behind the compressor in direct proximity to the hot turbine side. The three-dimensional turbomachinery structures were manufactured by conventional computer numerical control milling. Stable combustion was demonstrated using liquefied petroleum gas and the prototype reached 280,000 RPM in self-sustained operation. However, due to bearing instability, no electric energy output was produced. In a later design, only 30 W output was reached at 50% design speed, while higher speeds had to be avoided as maximum TIT was surpassed.

Other groups contributed to UMGT research on component level, without developing a functioning prototype. A group from von Karman Institute for Fluid Dynamics conducted theoretic cycle research on a recuperated gas turbine concept with an enhanced output target of up to 1000 W [16]. A target pressure ratio of 3 at a mass flow rate of 20 g/s was defined for a rotational speed of 500,000 RPM. The preliminary design disregarded global interdependencies between heat transfer effects, component and cycle efficiencies and rotordynamic behavior, which were addressed separately. In following, to allow high TITs, a 20 mm diameter turbine wheel was manufactured from silicon nitride by electric discharge machining. Subsequent conjugate heat transfer (CHT) studies revealed that due to heat flux from turbine to compressor, compressor efficiency may drop by 2% [17]. Despite intensive experimental investigations and application of different bearing configurations [18], only 240,000 RPM were reached due to low bearing stiffness, whirl instability and very tight air bearing clearance. System level testing was not accomplished, with main drawbacks being the bearing instability and the multipart rotor, which introduced additional imbalance and complexity.

In 2003, a group from Stanford University published their efforts toward UMGT with a monolithic ceramic rotor, manufactured by gel casting [19–22]. The system was designed to use air bearings to reach rotational speed of 800,000 RPM at TIT of 1273 K. Cantilevered configuration was chosen to place the bearings next to the generator on the engine cold side. In a cold gas test, the rotor was equipped with conventional roller bearings and reached 420,000 RPM before facing rotordynamic instability. Monolithic ceramic rotor has a significant advantage as no connecting bolts, threads, or press-fits are needed during assembly, rotor balancing is simplified and assembly of high speed parts is avoided. However, the proposed manufacturing technology was not viable since individual fugitive-wax mold assemblies and solder-masks needed to be machined and aligned for each part. This not only resulted in time-consuming and high cost processes, but also bore the risk of geometrical inaccuracy due to mold assembly misalignments.

In addition to these experimental works, a research group from Office National d'Etudes et de Recherches Aérospatiales published preliminary estimations on the heat transfer effects in a gas turbine with 10 mm rotor diameter. A novel two-stage turbomachinery configuration with a central combustion chamber was investigated [23]. Subsequent computational and experimental efforts focused on a single-stage UMGT system with 2D turbomachinery geometry, aiming for 50–100 W power output [24]. The target rotational speed of 840,000 RPM necessitated aerodynamic gas bearing development and to the best knowledge of the authors, air bearing operation has not been demonstrated yet.

The various prior studies and the reasons behind their discontinuation are summarized in Table 1. In light of previous research, three major obstacles can be identified on the path toward successful UMGT development:

(1) Previous projects addressed cycle efficiency, heat transfer, component efficiencies, and rotordynamics separately during the preliminary stage, and constraints were formulated on a component level rather than on a system level. Thus, in all reviewed contributions, pressure ratios of 3 and above were selected without considering the interdependency between the desired output power, component efficiencies, and rotordynamics. Moreover, in most cases, generator design was also not integrated in the preliminary stage.
(2) The bearing technology was selected to provide high rotational speeds for pressure ratios of at least 3. To avoid rotordynamic instabilities, one bearing was usually placed close to the hot turbine side, necessitating air bearing technology to simultaneously sustain high speed and temperature. However, the literature review shows that despite low friction losses and enhanced engine lifetime, air bearing technology was unsuitable for UMGT development as all prototypes failed to reach design speeds.
(3) The used manufacturing methods resulted either in low component efficiencies and volumetric flow rates for 2D turbomachinery structures, or in excessive manufacturing costs and

Table 1 Summary of previous UMGT projects

Research group	Design speed (kRPM)	Achieved stable speed (kRPM)	>Manufacturing technology and material	Configuration (x = bearing, C = compressor, T = turbine, G = generator, cc = combustor)	Reasons for discontinuation
MIT	2000	—	Deep reaction ion etching (Silicon, 2D)	Rotor outer diameter as air bearing	Heat transfer, manufacturing, bearing instability
Tohoku	870	360	Conventional machining (Titanium alloy, 3D)	CxGxTcc	Hydro-inertia bearing instability (whirl)
Korea Institute of Machinery and Materials	400	280	Conventional machining (Inconel 718, 3D)	xGCxTcc	Air bearing imbalance, system start-up
von Karman Institute for Fluid Dynamics	500	240	Electric discharge machining (Silicon nitride/Titanium alloy, 3D)	xGCxTcc	Air bearing instability
Stanford	800	420	Gel casting (Silicon nitride, 3D)	xGxCTcc	Rotordynamics, manufacturing
Office National d'Etudes et de Recherches Aérospatiales	840	500	Conventional machining (No material specified, 2D)	CxxTcc	Air bearing development, manufacturing

unreliable or time-consuming processes for 3D designs. Thus, a different manufacturing technology must be sought.

Motivation

In an attempt to alleviate these issues, the present UMGT development effort proposes several strategies to generate a viable conceptional engine design. Critical engine parameters, and particularly mass flow-dependent component performance, need to be addressed in a preliminary stage. Instead of striving for highest feasible pressure ratio, optimum pressure ratio evaluation is proposed based on system level constraints. To highlight parameter interdependencies, an analytic engine model is developed to include thermodynamic cycle, heat transfer, component efficiency, and rotordynamic analyses. In addition to that, in order to avoid the complications imposed by air bearings, the sustainable rotational speed of conventional ball bearings is set as a system constraint. As this technology requires reduced shaft temperatures for sufficient bearing lifetime, a cantilevered configuration must be chosen. Finally, toward efficient reduction of bearing temperature as well as heat flux from turbine to compressor, additive manufacturing is proposed to create an internal rotor cooling system. The current stage of additive manufacturing technology for small scales allows to produce monolithic UMGT rotors at reduced process complexity and cost. To the best knowledge of the authors, the geometrical flexibility of additive manufacturing has not been investigated for UMGT production and implied constraints and benefits have not been evaluated before.

Bearing Technology System Constraint

The rotational speed of previous UMGT concepts directly resulted from a design point in cycle analysis, desired output power, and optimum compressor work and flow coefficients. Therefore, the rotational speed was, in certain limits, not regarded as a system constraint parameter, leading to excessive speeds and selection of unreliable bearing technology. Hence, an inverse approach was chosen in the scope of the present project.

Modern ball bearing technology is widely used in dental applications, where speeds are reaching up to 500,000 RPM. In this operating setting, lifetime lubrication is commonly provided by specifically developed grease. However, high speed dental bearings cannot operate at elevated temperatures due to synthetic bearing cages. Therefore, before proceeding with UMGT cycle design, bearing system constraints are defined in coordination with a precision bearing manufacturer. According to bearing lifetime analysis (described in detail in the Appendix B), continuous operation of over 100 h at rated speed can be ensured if the shaft is cooled to approximately 80 °C.

This constraint necessitates cantilevered engine configuration and advanced heat transfer management. While the stator bearing casing can be cooled by the compressor inlet air, the rotor shaft temperature rise is driven by heat conduction from turbine to compressor. Therefore, a massive monolithic ceramic rotor would experience unacceptable shaft temperatures [22]. Thus, additional internal cooling of the rotor is necessary and will be addressed by additive manufacturing of internal cooling structure. Overall, the constraints for conceptional UMGT design that stem from selected ball bearings are:

- Cantilevered engine configuration,
- Design point speed: 500,000 RPM,
- Shaft surface temperature: 80 °C
- Shaft diameter: 4 mm.

Holistic Thermodynamic System Design

In the scope of the present project, the system-level constraints serve to determine the component design for maximum electric efficiency and rotordynamic stability. To provide a reliable prediction of component polytropic efficiency, commercial meanline turbomachinery design software (ANSYS VISTA) is coupled with the diabatic cycle calculation to form an analytic engine model. The diabatic thermodynamic simulation is described in detail in Appendix C. The amount of heat addition to compression and expansion is a fixed fraction of the polytropic process enthalpy change, determined based on literature data. In combination with the thermodynamic cycle model, the meanline software provides compressor and turbine geometries with optimum efficiency for the desired inlet temperature, pressure, mass flow rate, and rotational speed. Several parameters are fixed to ensure comparable design for different volume flows. For the compressor, the inlet hub radius is set to 4.5 mm, the back-sweep angle is 45 deg, and 14 blades (seven main and seven splitter) are selected with a tip clearance of 0.1 mm.

The inlet data are prescribed by ambient conditions and inlet pressure drop, while the total to total pressure ratio changes with the cycle analysis. Turbine blade speed ratio, incidence angle, diameter ratio and blade height ratio are selected in agreement with radial turbine design guidelines, using a tip clearance of 0.2 mm [25,26]. Turbine inlet conditions stem from the compressor outlet pressure and pressure drop in the combustor, as well as TIT, while the outlet pressure loss and the ambient conditions define the expansion ratio. Starting with initial guesses for component efficiencies, the specific electric power output is determined, and subsequently, the necessary mass flow rate to reach the defined electric power is calculated. The new mass flow rate is then imposed in the coupled meanline component software to

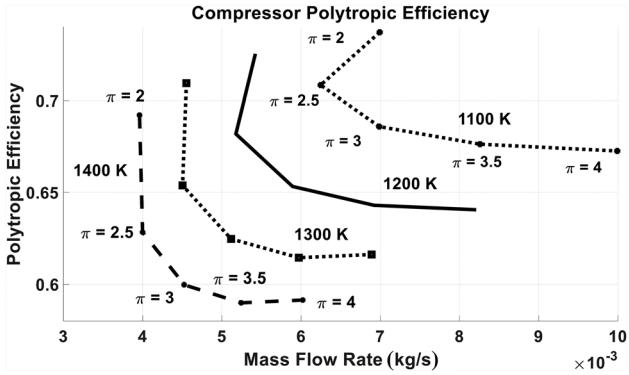

Fig. 2 Compressor efficiency for 300 W UMGT

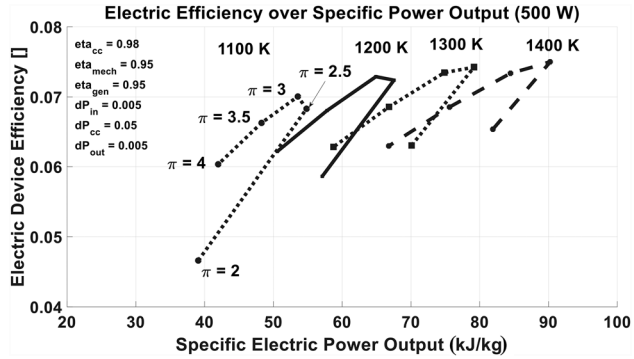

Fig. 4 Cycle analysis for 500 W UMGT

determine polytropic performance for the given parameters. By iterating this process, polytropic efficiencies and electric power converge into a realistic estimation of electric system efficiency. The results of this coupled cycle analysis show the importance of global design approach during preliminary UMGT development.

Figure 2 charts the compressor efficiency for different cycle pressure ratios in a 300 W system. Each line represents the cycle analysis results for a certain TIT. The polytropic total to total efficiency ranges from 58% to 75% depending on the mass flow rate. Looking at this data, it becomes clear that reduction of pressure ratio and TIT increases compressor efficiency and vice versa. This is due to the relatively low operational speed and mass flow rate that result in low compressor flow coefficient. The turbine efficiency is much less dependent on mass flow rate, with the efficiency range of 71–74% in all calculated cycle points.

The cycle calculation results for a 300 W UMGT are depicted in Fig. 3, where peak attainable electric efficiency is approximately 6.5%. Different TITs do not have a significant impact on cycle efficiency. This can be explained by a higher specific power, which consequently results in a lower mass flow rate for same wattage and thus lower compressor efficiency. The electric efficiency has a distinctive peak at a pressure ratio of 2.5, and thus, even though component efficiency for a pressure ratio of 2 is higher, the aggregate effect of low pressure ratio on cycle efficiency turns the balance and reduces the electric efficiency.

Increasing electric power output to 500 W also enhances the compressor flow coefficient and hence component efficiency rises. Figure 4 shows that this directly results in higher cycle efficiency at higher pressure ratios. For low TIT, electric efficiency is slightly higher for a pressure ratio of 3 compared to a pressure ratio of 2.5. However, as TIT increases, specific power output rises accordingly, resulting in lower mass flow rate and decreased compressor efficiency at higher pressure. Moreover, when comparing the 300 W and 500 W cases, it is noticeable that the electric efficiency drop for reduced pressure ratio of 2 is much larger in the 500 W system. This can be explained by reduced efficiency gain from higher mass flow rates as the compressor efficiency for a pressure ratio of 2 drops due to an excessive flow coefficient.

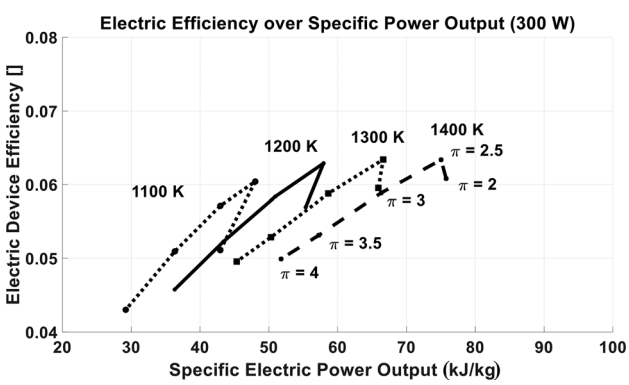

Fig. 3 Cycle analysis for 300 W UMGT

The results of this section imply that a system-level design approach can reveal a more realistic optimum cycle efficiency, when compared to a pure thermodynamic investigation. The findings relevant for UMGT development can be summarized as follows:

- Increasing pressure ratio beyond 2.5 does not result in significant performance improvement,
- Increasing TIT above 1300 K will reduce mass flow rate, but will not improve electric efficiency.

As a 500 W electric power output results in a larger combustion chamber and generator, a 300 W system with a pressure ratio of 2.5 and TIT of 1200 K was selected for further evaluation and conceptual design. This configuration is then calculated to have a mass flow rate of 5.2 g/s with estimated polytropic compressor and turbine efficiencies of 68% and 72%, respectively. Compressor and turbine diameters are 17 and 17.2 mm, respectively.

Materials and Manufacturing Technologies. After specifying rotational speed and obtaining geometry constraints for a 300 W UMGT system, different materials and manufacturing technologies can be considered for the gas turbine rotor. Due to centrifugal forces, maximum technical work of a turbomachine ($w_{\mathrm{tec,max}}$) is limited by the square root of tensile strength over density of the used material, denoted as reduced specific strength [5]

$$w_{\mathrm{tec,max}} \sim \sqrt{\frac{TS}{\rho}}$$

It is desirable to use materials with high specific strength, as this results in lowered centrifugal stresses for the same turbomachinery work input. Along these lines, Fig. 5 compares ceramic materials available or in advanced development for additive manufacturing and metal alloys frequently used in aerospace applications [27–30]. As commonly accepted, ceramic material strength is described by flexural strength instead of tensile strength. The data demonstrate that ceramic materials have similar reduced strength values as modern super alloys and may even outperform them in high temperatures.

Ceramics are not commonly used as blade or disk material in conventional turbomachinery due to statistically distributed material defects that result in low survival probability of large parts. However, ceramics are suitable for small-scale turbomachinery due to the reduced part volume which dramatically increases survival probability and reliability [21]. Same authors also developed a rapid prototyping technique for ceramic monolithic rotors [22]. However, this technology is not considered suitable for mass production or prototype development as several sacrificial wax mold components need to be machined and aligned for each part, resulting in costly and inaccurate production of individual rotors.

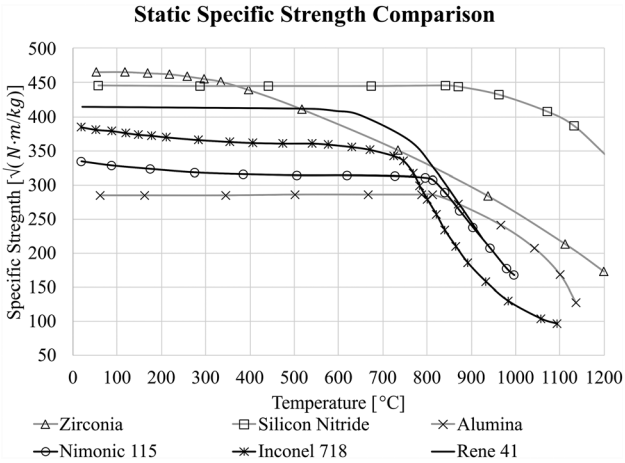

Fig. 5 Comparison of specific strength for ceramics and metals [27–30]

In contrast to this, dense ceramic parts can be produced efficiently and accurately by lithography-based ceramic manufacturing (LCM). In this process, frequently used in industrial and medical applications, the green body is generated by a UV-light mask, projected unto the build plate to solidify a thin layer of photopolymeric binder mixed with ceramic powder. Subsequently, the green body is debinded and sintered in a thermal process that is fine-tuned according to the desired material properties. Today, LCM is a well-proven industrial standard for alumina and yttria-stabilized zirconia [31], while pure silicon nitride technology is being developed [32]. Silicon nitride offers high strength, temperature and corrosion resistance, high thermal shock resistance, low density [33] and has already been implemented in radial turbine geometries [34]. However, according to international service providers, the process maturity of additive manufacturing is still low due to green body deformation and crack formation during the sintering process.

Zirconia is a technical ceramic, commonly stabilized with addition of yttria to yield high room temperature strength, very low heat transfer coefficient and similar to steel heat expansion coefficient. The high strength of this material results from a transformation toughening mechanism that prevents crack propagation and thus creates a more ductile behavior [35]. At high temperatures, this effect is reduced and a phase change with associated volume increase occurs depending on the yttria mole fraction. Zirconia thermal shock resistance is better than alumina and may be sufficient for small-scale parts. Printing zirconia with LCM technology is a mature process, reaching material properties similar to conventional ceramic manufactured components [32].

Alumina is commonly used in environments of up to 1600 °C, but suffers from thermal shock susceptibility. However, this effect is mitigated with scale and therefore alumina has also been suggested as rotor material for UMGTs [4]. Furthermore, thermal shock is usually tested by quenching hot parts in water, a procedure that is not representative for gas turbine operation. Instead, a study on thermal shock of alumina in heated air atmosphere by Panda et al. indicates that millimeter scale alumina parts may withstand a shock temperature gradient of up to 700 K [36]. Similar to Zirconia, LCM of alumina parts is a well-known process, that is widely applied in industry and can reach high surface quality and dimensional accuracy.

Common lateral resolution of LCM printers before sintering is 25 μm with a layer height of 10 μm [31]. Minimum feature size for commercial LCM technology is 0.1 mm and less. The surface roughness is reaching values below 1 μm Ra and dimensional accuracy of LCM is usually around $\pm 2\%$, with a minimum of ± 0.1 mm. Higher accuracy can be achieved by iterative process optimization for a selected geometry.

Beside the specified ceramics, Inconel 718, a common material in turbomachinery applications, is also available for additive manufacturing via selective laser melting (SLM) process. The effects of SLM manufacturing parameters on Inconel material properties are reviewed in Ref. [37]. Despite open pores, hollow cavities, material inhomogeneity and bonding defects, in some cases, the properties of SLM manufactured Inconel 718 can outperform the values of cast parts. However, commercially available SLM processes typically produce relatively low surface roughness and require large minimum feature size [38]. Alternatively, microlaser sintering (MLS) is known to have precision of ± 5 μm, resolution of 15 μm and layer height as low as 5 μm, while also offering outstanding surface roughness and minimum feature size when working with stainless steel [39]. However, this technology is not yet available for Inconel 718.

The potential materials for manufacturing UMGT rotors, along with their minimum feature size, resolution, and surface roughness are summarized in Table 2.

When applied to UMGT development, the following conclusions can be drawn from the materials and manufacturing technologies review:

(1) Lithographic-based ceramic manufacturing is a mature process for alumina and zirconia—two materials, which are not typically used in turbomachinery applications. Applicability for small scales has to be proved. High accuracy and surface finish can be achieved, and with iterative process adaption, postprocessing might be unnecessary to reach a tip gap of 0.1 mm. Minimum blade thickness can be as low as 0.1 mm.
(2) Selective laser sintering currently offers high temperature resistant material, but poor surface quality, feature size and accuracy. Blade thickness must exceed 0.3 mm and sandblasting is necessary. To reach turbine and compressor tip gap of 0.1 mm, additional postprocessing of the contour may be essential.
(3) LCM for silicon nitride as well as MLS for Inconel 718 have great potential for micro gas turbine applications, as in both cases, superior material properties are combined with high manufacturing performance.

Despite the enhanced geometrical flexibility of additive manufacturing, the layer-by-layer processing imposes constraints on the gas turbine rotor structure, which are reflected in design guidelines [40,41]. The maximum contour slope is limited in the direction of manufacturing to ensure stability of the overhung material. Maximum overhung angles depend on the layer height and process parameters and usually should be below 40 deg–60 deg, without additional supports. Using support structure is a solution to

Table 2 Available materials and processes

	Process	Minimum feature size (mm)	Resolution (μm)	Surface roughness (μm Ra)	Process maturity
Alumina	LCM	0.1	25	0.4-0.6	Industrial standard
Zirconia	LCM	0.1	25	0.3	Industrial standard
Silicon nitride	LCM	0.1	25	0.3	In development
Inconel 718	SLM	0.3	40	6.5	Industrial standard
Inconel 718	MLS	0.05	5	1	Not yet available

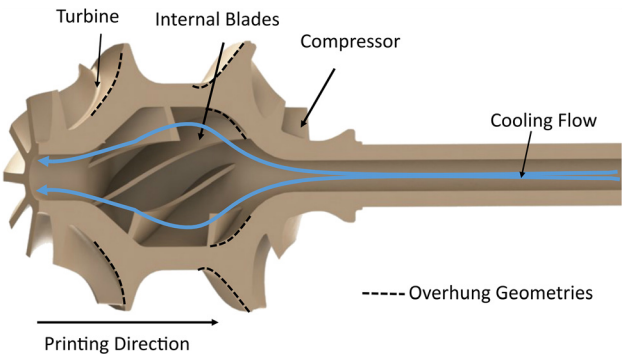

Fig. 6 Preliminary rotor design

this constraint, however it significantly impacts surface quality and thus flexural strength of ceramic structures. Besides limited slope, additive manufacturing also requires a flat surface at the build plate. The suggested monolithic impeller geometry is designed in accordance with these limitations. To ensure build plate adhesion, the radial turbine trailing edge is cut back, establishing a flat surface at the lower end of the rotor.

The described guidelines are also considered for the monolithic turbine rotor geometry with internal bladed cooling cavity. This shaft architecture has several system benefits. The internal flow generated by reduced outlet pressure decreases turbine to compressor heat flux and cools the bearing and generator surfaces. The latter effect is essential to realize the proposed conventional bearing technology, which requires low shaft temperature. Moreover, the shaft stiffness is improved as material is removed from the middle and shifted to the outer diameter of the rotor. This way, the bending mode frequency is increased, enabling operation below bending modes. In addition to that, the internal flow creates structural cooling of the turbine, easing material requirements. Finally, the internal cavity results in less material agglomeration and enables a more homogeneous sintering process. The resulting rotor geometry is presented in Fig. 6.

Rotordynamic Performance. To evaluate the effect of potential materials and manufacturing methods on UMGT performance, alumina, zirconia, silicon nitride, and Inconel 718 are assessed in a comparative rotordynamic study. Figure 7 shows the simplified rotordynamic model used to investigate the effect of geometric parameters on mode frequencies. The rotor suspension is modeled by using roller bearing stiffness at operating speed, as provided by the manufacturer. To avoid critical modes during operation, the mode frequencies should have a safety margin of 20% from the operating frequency. The modal analysis was conducted using ANSYS Modal toolbox.

The permanent magnet dimensions are estimated using an analytic optimization [42] (described in detail in Appendix D). Starting from a baseline geometry, the magnet length (L) and diameter (D) are varied according to seven valid ratios calculated with the generator design code. To ensure operation without excessive vibrations, the bending modes of the structure must be avoided by scaling the generator within the allowed geometry resulting from this calculation.

Usually, the first bending mode is critical for overhung rotors as the free end is deformed close to the bearing causing fatigue load on the shaft [43,44]. The analysis results show that the first mode is a rigid body mode due to the relatively low bearing stiffness at high speed. The second mode (first bending mode) occurs at approximately 50% of the operating frequency and transitions into a rigid body mode for lower length over diameter ratio and for higher material stiffness over density ratio. For longer shafts, this mode may turn into a bending mode as well. The third mode of the system is a structural bending mode of the rotor. Figure 8 describes the second and third modes for a zirconia rotor with a

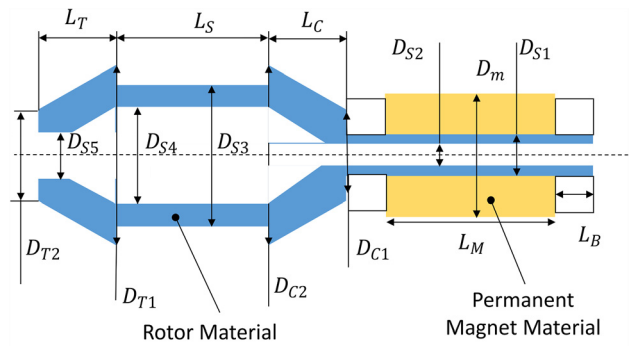

L_B	L_M	L_C	L_S	L_T
2 mm	L (varies)	7 mm	8 mm	6 mm
D_{S1}	D_{S2}	D_{S3}	D_{S4}	D_{S5}
4 mm	1.5 mm	10 mm	8 mm	2 mm
D_{C1}	D_{C2}	D_{T1}	D_{T2}	D_M
4.5 mm	17 mm	17.2 mm	5.6 mm	D (varies)

Fig. 7 Simplified rotordynamic engine model and relevant dimensions

permanent magnet length to diameter ratio of 1.68. This setup is marked as reference point in Fig. 9, which summarizes the findings of the rotordynamic analysis for different materials. It is obvious that while the second mode may be crossed during start-up, the third mode must be avoided due to excessive shaft deformation.

Figure 9 shows the second mode forward whirl and third mode backward whirl frequency progression for different length over diameter ratios and materials. The third mode frequencies are observed to be affected stronger than the second mode. With increased L/D ratio, the third mode frequency is reduced as the bearing distance is longer. Furthermore, the material stiffness to density ratio has a great impact on the resulting bending mode frequencies. The results also show that the second bending mode is far above the operating frequency range for alumina and silicon nitride due to their high stiffness and low density. Compared to this, zirconia and Inconel 718 show bending mode frequencies closer to the operating range. Therefore, a lower length to diameter ratio must be selected for Zircoina and Inconel to avoid interference with the second bending modes during operation. However, this approach is limited, as the stress at the permanent magnet inner radius rises quadratically with the outer radius [45], necessitating a tight fit between the permanent magnet and the containing sleeve [46]. This requires a thicker sleeve which in turn reduces generator efficiency. Moreover, the bearing distance should be as large as possible for practical reasons of the balancing procedure. It is therefore desirable to keep the L/D ratio as high as possible, resulting in a conflict of objectives with the rotordynamic performance.

To this end, the L/D ratio values differ from material to material and are selected to be as large as possible, but without interfering the safety margin, Table 3. It can be summarized that silicon nitride and alumina are at this point most desirable materials from a rotordynamic and generator design perspective.

Combustor Concept. Different combustor concepts have already been demonstrated in prior UMGT development efforts. In the scope of this work, premixed combustion in a porous inert media is used to establish a high power density burner. Porous media combustion of liquid and gaseous fuels has been suggested for microgas turbine systems due to high energy density, favorable turn-down ratios, and stable burning. The porous material causes turbulent flow, which contributes to stable combustion even at higher flow speeds [47]. When facilitating premixed combustion, the low equivalence ratios necessary for the desired TIT in a range of 1100–1400 K are challenging. Porous media

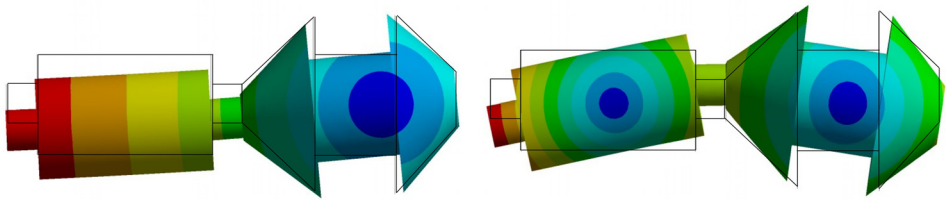

Fig. 8 Second (left) and third (right) mode deformation

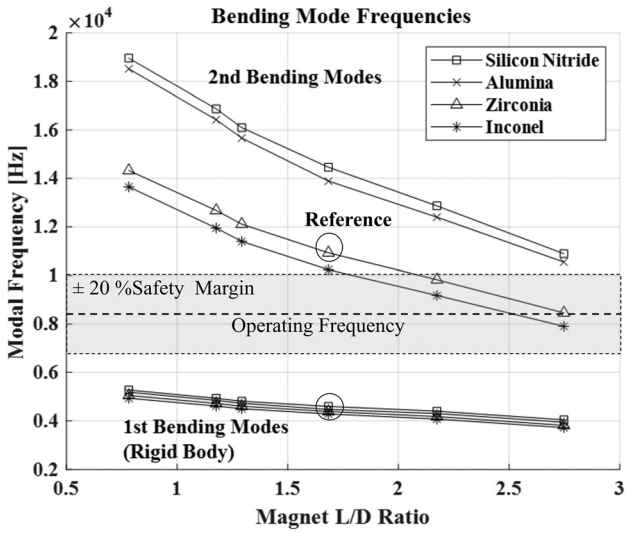

Fig. 9 Rotordynamic behavior of the simplified geometry for different materials

combustion offers a viable solution to this problem, as the radiative heat transfer within the material preheats the reactants and subsequently allows higher flame speed and lower equivalence ratios. Equivalence ratios as low as 0.3 with resulting outlet temperature of 1100 K have been demonstrated experimentally with porous media burners for liquid and gaseous fuels [47–52]. Radial burners have advantage over axial burners, as the flow speed varies with radius. This results in a stable flame front, with experimental data suggesting flow speed of about 8 m/s for stoichiometric conditions [47].

However, if high amount of excess air is to achieve temperatures below 1300 K, the bulk flow velocities must be in the range of 1–3 m/s [49]. This is challenging in a microgas turbine application as diffuser exit flow velocity is usually an order of magnitude higher. Moreover, high velocity flow through the porous media results in excessive pressure drop, conflicting with the design guidelines formulated in the cycle sensitivity analysis (described in detail in Appendix E). Therefore, the porous media inlet area must be significantly increased to ensure stable combustion and low pressure drop. This can be achieved by a radial inward-directed flow that is wrapped around the porous material. The fluid exiting the compressor is directed to a recirculation jacket, similar to the design proposed by MIT [4]. In this channel, the air is partially preheated as it passes next to the hot porous media. As the porous material creates flow resistance, the fluid enters the combustor with homogeneous velocity distribution. For a discharge density of 2 kg/m^3 and a mass flow rate of approximately 6 g/s, the necessary surface area is 1000 mm^2.

Regarding the pressure drop, estimations can be made based on a flat flame burner [50], where total inlet pressure loss of 2% was measured at a flow velocity of 2 m/s and porosity of 50%. 5% pressure drop assumption is therefore in line with experimental data for low velocity flow.

Table 3 Selected *L/D* ratio for different materials

Material	*L/D* ratio
Inconel 718	1.68
Silicon nitride	2.2
Alumina	2
Zirconia	1.68

Conceptional Ultramicrogas Turbines Design. At this point, the turbomachinery geometry as well as the bearing positions, shaft dimensions, and permanent magnet geometry are determined via the preliminary design process and the system layout of the engine configuration is portrayed in Fig. 10. The premixed air and fuel enter the engine radially through the intake and are compressed in the centrifugal compressor. During subsequent diffusion, heat from the combustor is transferred to the flow to preheat the mixture. The porous media combustor is then enclosed by the incoming mixture and a flame at the outer radius of the porous material (region of the lowest flow velocity) is established. The hot gases propagate radially inward toward a hollow cavity prior to entering the guide vanes of the radial turbine. The flow is then further heated by the additional mixture that enters the porous media from the inner radius.

To provide sufficient cooling for the radial bearings, as well as compressor and turbine structure, cooling flow enters the hollow rotor at ambient conditions in front of the generator.

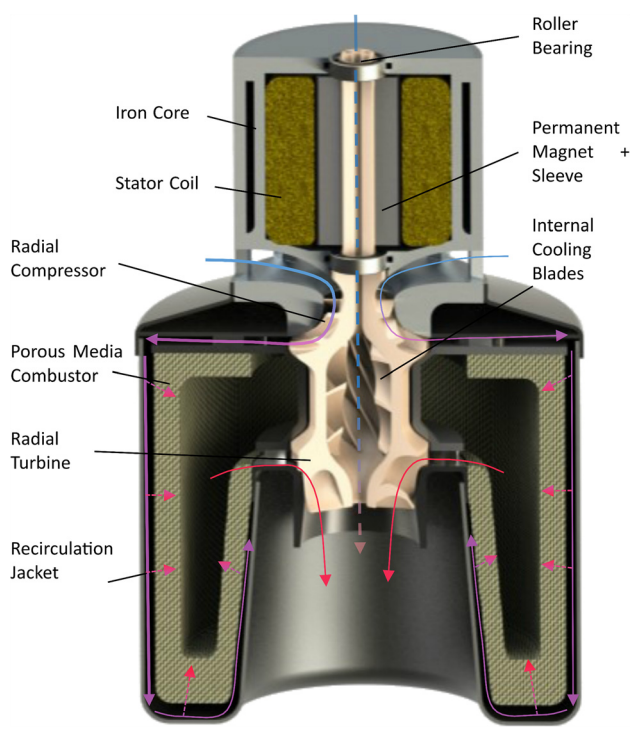

Fig. 10 Conceptual UMGT engine architecture

Subsequently, heat exchange takes place with the structure and material temperatures are reduced.

In comparison to previous research projects, the following novelties and advantages are presented in the current design:

- Rotor design that exploits full potential of additive manufacturing technologies,
- New cooling strategy by internal flow,
- Reliable and well-known bearing technology,
- Rotordynamic stability due to enhanced shaft stiffness,
- Optimized pressure ratio with respect to cycle performance,
- Premixed porous combustor architecture.

Preliminary Computational Fluid Dynamics Results. To evaluate the validity of the preliminary stage assumptions, computational fluid dynamics (CFD) simulations and CHT calculations are performed using ANSYS CFX solver. CFD analysis is conducted for the meanline radial compressor geometry at rotational speed of 500,000 RPM, pressure ratio of 2.5 and mass flow rate of 5.2 g/s. To reduce the root stresses, the blades are designed with a hub fillet of 0.15 mm radius. As minimum wall thickness of SLM process is limited to 0.3 mm, the blade root thickness varies from 0.44 mm to 0.55 mm. The clearance between casing and compressor is set to 0.1 mm. The compressor has elliptic leading and trailing edge geometries, as suggested in Ref. [53]. The diffuser geometry is optimized within the boundaries of geometrical guidelines [54], based on a screening method. A radial intake is integrated in the model according to the engine architecture.

The ANSYS CFX internal wall function model is applied in combination with k-ε turbulence and a y^+ value of 30—an approach proposed and validated in Ref. [55]. The k–ε turbulence model is known to have good agreement with experimental data for mesoscale turbomachinery [20]. ANSYS TURBO-GRID is used for discretization, resulting in a compressor rotor section mesh with 640,000 elements and diffuser section mesh with 440,000 elements. The two domains are interfaced by a mixing plane model, conserving total pressure. Inlet total state and outlet mass flow are selected as boundary conditions. Heat capacity and transport properties are implemented as function of local temperature. To evaluate the applicability of proposed additive manufacturing methods, different sand grain size values are set on the rotor surface to simulate roughness according to Ref. [56].

Computational fluid dynamics findings for the compressor stage are charted in Fig. 11 in terms of velocity contours, while the results of all simulations are summarized in Table 4. The comparison of sand grain sizes associated with the proposed additive manufacturing techniques shows that compressor efficiency is reduced by approximately 1% for an SLM process value of 34.5 μm Ra, when compared to the very smooth surface of LCM technology. Therefore, LCM technology is most desirable but not crucial for sufficient compressor efficiency. Moreover, the pressure ratio is hardly affected by surface roughness change. Finally, the compressor polytropic efficiency is predicted with reasonable accuracy by the meanline software (68% for a pressure ratio of 2.5 and a mass flow rate of 5.2 g/s). This value can surely be reached with additional rotor and diffuser optimization, which are out of this paper's scope. In similar fashion, turbine CFD calculations yield polytropic total to static efficiency of up to 72%.

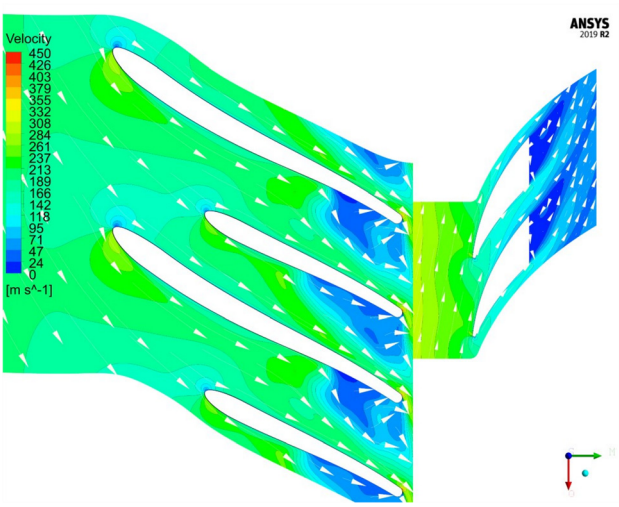

Fig. 11 CFD results for the compressor stage—velocity contours

In following, CHT analysis is conducted in ANSYS CFX to evaluate the temperature distribution within the hollow rotor. The model, depicted in Fig. 12, consists of three domains for rotor structure, cavity flow and gap flow. Solid and cavity domain are full models with unstructured meshes of 235,000 and 620,000 elements, respectively. The gap fluid domain is a 5 deg section with a structured mesh of 50,000 elements. To capture the boundary layer heat transfer from solid to fluid domain, inflation layers are applied to reach y^+ of 1 at the fluid-solid interfaces. As fluid and solid meshes are not matched, the solid mesh is refined at the boundary to reduce interpolation error. Since this paper focuses on the internal heat exchange between cavity and solid, the heat transfer at turbine and compressor surface is simplified by applying the Sieder–Daast equation with averaged temperatures and heat transfer coefficients. This approach was demonstrated to be in good agreement with a full conjugate model in a microgas turbine scenario [17].

The cavity inlet conditions are prescribed by ambient total pressure and static temperature. At the cavity domain outlet, the turbine exhaust flow causes an entrainment effect on the internal cavity, owing to the lower static pressure induced by high turbine outlet velocity. To capture this effect, the outlet conditions of a separate radial turbine simulation are interfaced with the cavity domain. Outlet pressure and temperature of the cavity domain are set according to ambient conditions. The gap flow domain is interfaced with the solid domain at the outer contour of the shaft. In this simulation, the parallel gap width is set to 0.1 mm, representing highest achievable manufacturing accuracy.

Inlet total pressure and outlet static pressure of the gap domain are found from compressor and turbine CFD simulations. Another boundary condition of this domain is the outer wall temperature. In a full CHT analysis of a UMGT (including stator and rotor) the gap wall temperature ranged from 600 to 750 K [57]. Therefore, a conservative value of 750 K is applied at the outer wall of the gap fluid domain. The conductivity of the used solid materials is implemented as a function of temperature. The CHT analysis is then conducted for the four selected materials and the results of the study are summarized in Table 5 in terms of generator shaft temperature and heat fluxes. The fluid and solid temperature fields for a sample material (Inconel 718) are visualized in UMGT cross section in Fig. 13.

The results indicate that the shaft temperatures are relatively high with respect to the limiting value of 80 °C, which is demanded for 100 h of continuous bearing operation. While the findings for zirconia and Inconel 718 indicate sufficient cooling of the shaft, alumina and silicon nitride may reduce bearing lifetime. Absent of cavity cooling, the solid shaft geometry would significantly increase shaft temperature. Therefore, additive manufacturing is considered not optional, but rather an essential technology to realize the proposed engine architecture.

Beside shaft temperature, heat fluxes in the compression and expansion processes are important as they affect the cycle efficiency. Heat flux values are very similar for alumina, silicon nitride, and Inconel 718. For these three materials, the heat transferred to the internal cavity is approximately half of the heat transferred to the compressor. Inconel 718 presents a slightly lower compressor heat flux value, which can be explained by the material's thermal conductivity that rises with temperature.

Table 4 Compressor CFD results for different materials

Material and process	Equivalent sand grain size (μm)	Stage polytropic efficiency	Pressure ratio
Alumina (LCM)	3.2	65.2%	2.48
Zirconia (LCM)	1.6	65.3%	2.47
Silicon nitride (LCM)	1.6	65.3%	2.47
Inconel 718 (SLM)	34.5	64.2%	2.43
Inconel 718 (MLS)	5.3	65.1%	2.45

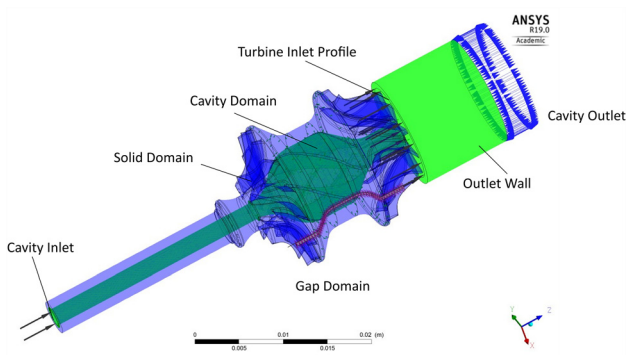

Fig. 12 Conjugate heat transfer simulation model

Compared to this, heat flux is significantly reduced for zirconia due to its low thermal conductivity. This has positive impact on cycle efficiency, but at the same time, structural temperatures are increased.

Using the compressor efficiencies tabulated in Table 4, the resulting cycle efficiencies are evaluated based on the analytic engine model. According to the preliminary investigation, pressure ratio and TIT are set to 2.5 and 1200 K, respectively. Other cycle properties such as combustor pressure drop, inlet pressure drop, and electric and mechanic efficiencies are prescribed according to the reference point cycle analysis (described in detail in Appendix F). The turbine polytropic efficiency is set to 72%. The obtained electric efficiencies are 5.1% for alumina, silicon nitride and both SLM- and MLS-manufactured Inconel 718, and 5.2% for zirconia. Zirconia has a small advantage due to low compressor side heat flux and high surface quality. It can also be noted that Inconel 718 printed with current SLM technology is competitive with silicon nitride and alumina, despite the lower component efficiency, as its compressor heat flux is reduced by approximately 15%.

Material Stress Estimation. In order to study the ability of different materials to withstand material stresses that develop in the UMGT model, an FEM simulation is conducted on the preliminary geometry using temperatures obtained from CHT analysis. The results are summarized in Table 6 in terms of turbine blade root stresses. Zirconia and Inconel 718 have comparatively high density, resulting in linearly growing centrifugal stresses. Compared to this, alumina and silicon nitride offer low density, resulting in minimum stress values. Moreover, the high thermal conductivities of alumina, silicon nitride, and Inconel 718 result in lower structural temperature on the turbine side, which is beneficial from a stress perspective. In contrast to this, zirconia shows higher structural temperature. Therefore, while low thermal conductivity is beneficial to reduce bearing shaft temperature, it may impose excessive thermal loads on the turbine.

The resulting stresses and temperatures are compared to material data for tensile strength of alumina [58], 3% yttria-stabilized zirconia [59], silicon nitride [60] and Inconel 718 [28]. The precise stress limits of the ceramic materials are difficult to predict based on literature data, as they depend on part geometry and sintering process. Thus, the values presented here are considered as conservative estimation for relevant temperatures. According to these data, alumina is unsuitable for the current geometry, as the maximum stress exceeds the tensile strength limit. Additional optimization is therefore necessary to facilitate this material. Zirconia is a viable option as a safety margin of almost 100 MPa can be expected. Silicon nitride outperforms all materials due to its low density and high temperature strength. Beside ceramics, Inconel 718 also shows sufficient safety margin.

Further FEM investigations on the entire rotor geometry show that compressor side stresses in the cavity currently surpass tensile strength of zirconia, alumina and Inconel 718 for the presented baseline geometry. However, multiparameter optimization of the internal cavity geometry is expected to significantly reduce stress

Table 5 Shaft temperature and heat fluxes for different materials

Material	Shaft temperature	Turbine (W)	Cavity (W)	Gap (W)	Compressor (W)
Alumina	99 °C	110.1	−34.7	−6.5	−68.9
Zirconia	72 °C	58.2	−25.0	−5.7	−27.5
Silicon nitride	94 °C	118.5	−37.6	−12.9	−68.1
Inconel 718	83 °C	117.7	−39.3	−19.5	−58.9

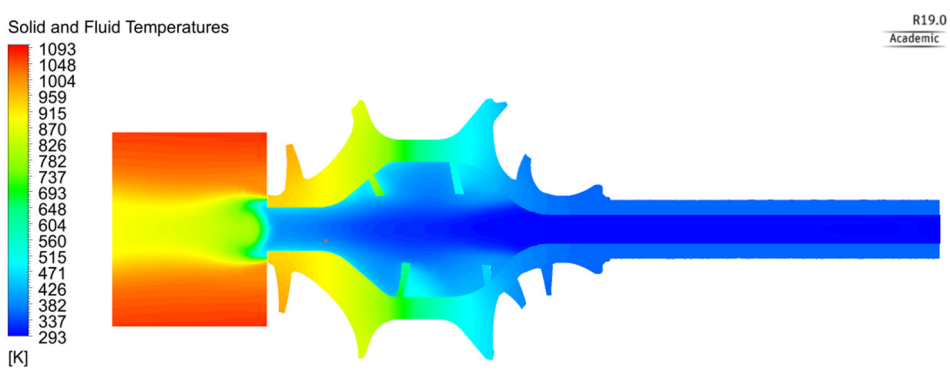

Fig. 13 Temperature distribution in fluid and solid domain for Inconel 718

Table 6 Stress and temperature at the turbine blade root

Material	Average blade root temperature	Estimated tensile strength	Turbine blade root stress
Alumina	685 °C	260 MPa	290 MPa
Zirconia	704 °C	540 MPa	442 MPa
Silicon nitride	681 °C	720 MPa	233 MPa
Inconel 718	679 °C	920 MPa	588 MPa

for these materials. Therefore, it is appropriate at the current stage to consider turbine blade root stress as a limiting factor.

Discussion

The preliminary design process of the monolithic gas turbine rotor reveals the effect of different manufacturing processes and materials on system level engine performance. At the current stage, silicon nitride is the most desirable material due to its excellent high temperature and strength capabilities. Moreover, the high stiffness and low density result in bending mode frequencies far from the operating range. This allows using a slim permanent magnet, which will reduce sleeve stresses and enhance generator efficiency. However, a silicon nitride rotor may result in elevated shaft temperature and thus reduced bearing lifetime. Moreover, additive manufacturing of this material is currently not available for the proposed complex geometry. Besides silicon nitride, zirconia offers a viable alternative with some compromises in the bending mode safety margin and maximum stresses. Due to its low thermal conductivity, the shaft temperature is reduced, and excellent bearing lifetime can be expected. Furthermore, cycle efficiency is increased. Inconel 718 shows high potential due to its high-tensile strength and lowered conductivity at high temperature, which results in acceptable shaft temperature. However, a large permanent magnet diameter is necessary to avoid bending mode frequency, which in turn will reduce generator efficiency. The study also suggests that alumina is not applicable to the current geometry due to its low tensile strength.

After elaborating on the UMGT design, the system weight can be predicted in a reasonable range. As the proposed technology is in competition with lithium-ion batteries for UAVs, a power density comparison is conducted based on the presented engine architecture. To that end, a hybrid electric energy supply system is envisioned to provide electric power output for a UAV, Fig. 14. As it is desirable to run the gas turbine at constant load, a battery buffer is connected to the UMGT. This way, electric energy produced can be stored and extracted on demand.

To estimate the battery buffer weight for a 300 W output system, the demanded time of autonomous flight in case of engine shutdown is set to 1 min. Suitable batteries, which weigh around 40 g, are commonly available for model aircraft applications. The overall system mass is estimated to be 291 g, with distribution according to Fig. 15.

Now, using the cycle efficiency, hydrocarbon energy density, and system weight, the energy density of the proposed system can be determined and compared to modern UAV lithium-ion battery technology. Energy density of a typical UAV battery with suitable power output is 150 Wh/kg and stored energy per unit mass can be considered to rise linearly [61]. In contrast to this, the UMGT system has an offset in stored energy due to the system weight. The additional stored energy is then increasing according to the energy conversion efficiency and fuel specific energy. As mentioned before, the expected UMGT cycle efficiency is 5.1% at a system weight of 291 g and a fuel energy density of 14.9 kWh/kg.

The resulting comparison in stored energy progression as a function of weight is depicted in Fig. 16. For the microgas turbine, energy density is a function of system weight due to the initial offset. Thus, in the evaluated design, an energy density enhancement factor of 3.6 can be reached in a 1 kg system, when compared to conventional lithium-ion batteries.

Conclusions and Future Work

The aim of this paper is to present in detail the preliminary design process of additively manufactured ultramicrogas turbines with conventional bearing technology. For the design of a 300 W microgas turbine, a system-level engine model is elaborated to highlight interdependencies between thermodynamic cycle, heat transfer, component efficiency, and rotordynamics. This analysis proves that mass flow-dependent turbomachinery component efficiencies result in significantly reduced optimum pressure ratio for maximum cycle efficiency. Based on the constraints implied by conventional bearings and desired electric power output, the optimum pressure ratio is determined to be 2.5.

A preliminary rotordynamic model is then used to optimize generator dimensions such that bending modes are avoided while the desired electric power output and efficiency are reached. Premixed porous media combustion is evaluated as a viable strategy to facilitate a high energy density burner. Finally, based on additive manufacturing limitations and material constraints, a novel hollow rotor architecture with internal cooling blades is presented.

Preliminary CFD results reveal the effect of manufacturing surface roughness on compressor efficiency, concluding that performance does not deteriorate severely for the investigated technologies. To estimate the impact of heat transfer on cycle efficiency, a conjugate heat transfer analysis for the hollow rotor structure is carried out for four different materials. It shows that depending on the material, electric efficiency of up to 5 percent can be reached. The study also suggests that while silicon nitride may be the most desirable material for the monolithic rotor, zirconia and Inconel 718 may offer viable alternatives.

The positive conclusions of the present effort present a clear path toward future multiparameter optimization of the monolithic

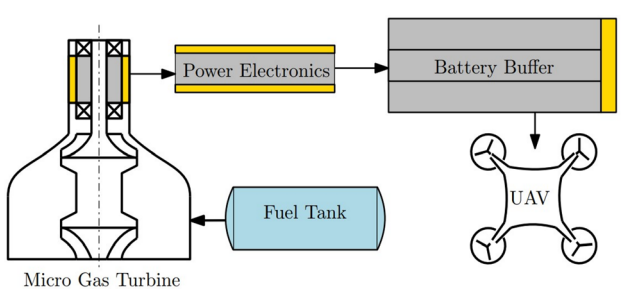

Fig. 14 Hybrid electric energy supply system

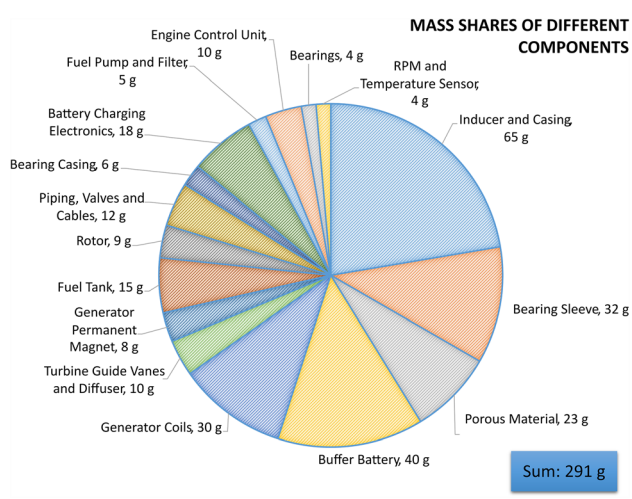

Fig. 15 System mass distribution

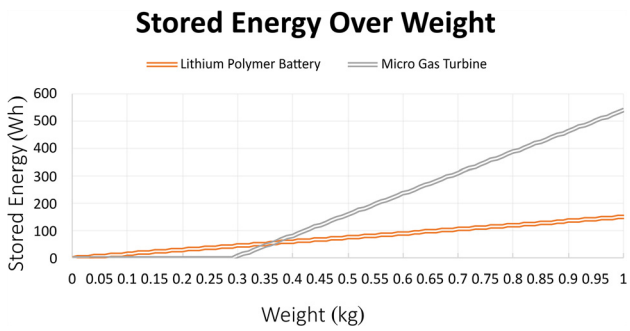

Fig. 16 Stored energy versus weight comparison

rotor with respect to component efficiency, heat transfer, rotordynamics and structural stresses. Moreover, the preliminary data gathered in the scope of this research allow for additive manufacturing of monolithic rotors from relevant materials, which would then be subjected to cold and hot gas tests. It is the hope of the authors that the combination of present findings and the future works will culminate in a demonstration of a functional additively manufactured gas turbine prototype with 300 W electric power output.

Acknowledgment

The present research effort was partially supported by Minerva Foundation (Grant AZ5746940764) and Meimad Grant of Israel Innovation Authority (Contract 68431). In addition, Research was sponsored by the Army Research Laboratory and was accomplished under Cooperative Agreement Number W911NF-20-2-0156. The views and conclusions contained in this document are those of the authors and should not be interpreted as representing the official policies, either expressed or implied, of the Army Research Laboratory or the U.S. Government. The U.S. Government is authorized to reproduce and distribute reprints for Government purposes notwithstanding any copyright notation herein.

Funding Data

- Army Research Laboratory (Cooperative Agreement No. W911NF-20-2-0156; Funder ID: 10.13039/100006754).
- Minerva Foundation (Grant No. AZ5746940764; Funder ID: 10.13039/501100001658).
- Office of the Chief Scientist, Ministry of Economy (Meimad Grant No. 68431; Funder ID: 10.13039/501100007171).

Nomenclature

Symbol Units

c_p = heat capacity at constant pressure (J/kgK)
D = diameter (m)
h = specific enthalpy (J/kg)
L = length (m)
P = pressure (N/m^2)
q = specific heat (J/kg)
r_q = heat flux ratio
T = temperature (K)
TS = tensile strength (MPa)
v = specific volume (m^3/kg)
w = specific work (J/kg)
η_p = polytropic efficiency
ρ = density (kg/m^3)

Subscripts

c = compressor
dia = diabatic
max = maximum
qc = compressor heat flux ratio
qt = turbine heat flux ratio
t = turbine
tec = technical

Abbreviations

CHT = conjugate heat transfer
FAR = fuel to air ratio
LCM = lithography-based ceramic manufacturing
MLS = micro laser sintering
SLM = selective laser melting
TIT = turbine inlet temperature
UAV = unmanned aerial vehicle
UMGT = ultramicrogas turbine

Appendix A: Unmanned Aerial Vehicle Weight and Battery Power Summary

The models and the relevant parameters of the drones used to chart Fig. 1 are summarized in Table 7. One of the UAVs (Power Vision's Power Eye) is relevant to both entertainment and field operation sectors and shows twice in the chart.

Table 7 UAV models and characteristics

Make	Model	Sector[a]	Maximal take-off weight (gr)	Battery power (W)[b]
Yuneec	Typhon H3	E	1985	218
Yuneec	Mantis Q	E	480	58
Yuneec	H520	E	1633	192
Yuneec	Typhon H Plus	E	1645	171
Yuneec	Tornado H920+	F	5000	445
DJI	Matrice 200	F	5800	450
DJI	Mavic 2	F	907	115
DJI	Spark	E	300	63
DJI	P4 Multispectral	F	1487	198
DJI	Inspire 2	E	4250	434
DJI	Phantom 4 RTK	F	1391	178
Parrot	Anafi	E	285	49
Parrot	Bluegrass Fields	F	1800	238
Parrot	Anafi Thermal	F	315	47
Ingegneria Dei Sistemi	IA-3 Colibri	F	5000	300
AeroVironment	RQ-11B Raven	M	1900	250
EMT	Aladin	M	3200	260
Microdrones	MD-1000	T	6000	360
Power vision	Power Eye	E, F	3950	400

[a]E—entertainment, F—field operation (inspection, mapping or surveying), M—military, T—transport
[b]Typically, not specified by manufacturer, estimated instead from specified flight time.

Appendix B: Bearing Lifetime Calculation

In order to estimate device efficiency, friction losses must be considered. Previously, dental bearings operating at 500,000 RPM were already used toward the development of a high speed generator with 100 W electric power output [46,62–64]. The mechanical bearing losses were evaluated experimentally at this speed to be approximately 10 W [63]. This value is also in line with the loss calculations for the selected bearings provided by the manufacturer. According to lifetime calculation done by bearing manufacturer, prescribing boundary conditions according to Table 8 results in a value of above 100 h.

Table 8 Ball bearing lifetime calculation parameters

Parameter	Value
Operating speed	500,000 RPM
Shaft temperature	80 °C
Axial preload	2 N
Axial load	5 N
Radial load	<1 N
Lubrication	Grease

Appendix C: Diabatic Cycle Analysis

A thermodynamic cycle analysis program is developed to highlight the effect of different parameters on UMGT performance. The program evaluates well-known ideal gas relations, as well as first and second law equations for changes of state. NASA polynomials are used to address the temperature dependency of heat capacity [65]. The program is separated into compressor, combustor, and turbine modules. The aerodynamic performance of turbine and compressor is determined using total to total polytropic efficiencies. Inlet and outlet pressure losses are considered as well as combustor pressure drop, combustion efficiency, mechanical efficiency, and generator efficiency. Adiabatic calculations are validated using data from Refs. [66–68]. To account for diabatic effects, heat flux in compressor and turbine is modeled as a constant fraction of the polytropic compression and expansion enthalpy change.

In small-scale gas turbines and turbochargers, heat flux from turbine to compressor results in performance deterioration. Heat flux as a function of pressure progression has a significant impact on component efficiency, as the compression work is increased due to diverging isobaric lines on T-S diagram. As pointed out in Ref. [69], the integration path of the diabatic process changes the temperature progression and with it the associated compression or expansion work. Introducing heat at a low pressure has a pronounced impact on compression efficiency, as more work is needed to pressurize high temperature fluid [70]. Therefore, compression at a higher temperature results in more work input than at low temperature. In contrast, adding heat flux at the end of the compression process is less harming to component efficiency, as most of the pressure change has already been accomplished. This effect is reversed for the turbine, where decreasing fluid temperature by cooling reduces available shaft work output.

This paper follows the approach applied in Ref. [71], where compression and expansion processes are divided into several steps. Thus, heat addition can be modeled as a function of pressure change. Along the streamline coordinate of the compressor, the wetted disk surface area, and hence heat flux, rises quadratically with the radius. Following Euler equation, total pressure is proportionate to the square of rotational velocity and thus also increases quadratically with the radius:

$$A_{\text{disk}} \sim q \sim r^2 \tag{C1}$$

$$P_t \sim u^2 \sim r^2 \tag{C2}$$

This way, linear heat addition with pressure rise can be justified, assuming constant temperature difference and heat transfer coefficient

$$\delta q_i \sim \delta P_{t,i} \tag{C3}$$

The diabatic change of state is now separated into incremental adiabatic compression with subsequent heat addition steps. The differential change of state can be discretized as

$$dh_{\text{dia},c} = dw_c + đq = \frac{vdP}{\eta_p} + đq \tag{C4}$$

$$\delta h_{\text{dia},ic} = \underbrace{\frac{\int_i^{i+1} vdP}{\eta_p}}_{\delta w_c} + \delta q_i(P_i) \tag{C5}$$

Similar formulation is used for the turbine, where the static outlet pressure is prescribed from ambient conditions and outlet pressure drop

$$\delta h_{\text{dia,it}} = \underbrace{\int_i^{i+1} vdP \cdot \eta_p}_{\delta w_t} + \delta q_i(P_i) \tag{C6}$$

To ensure comparability of specific heat flux, global component heat flux is given as a fraction of the polytropic pressure change in the components

$$q_{\text{global},c} = \int_{1_{\text{total}}}^{2_{\text{total}}} vdP \cdot r_{qc} \tag{C7}$$

$$q_{\text{global},t} = \int_{1_{\text{total}}}^{2_{\text{total}}} vdP \cdot r_{qt} \tag{C8}$$

Using this formulation, higher pressure ratios, as well as higher inlet temperatures, result in more heat flux from compressor to turbine. This is in agreement with turbomachinery design, as higher pressure ratios cause higher tip speeds and hence larger diameters for the same rotational speed. Moreover, a lower pressure ratio enhances the mass flow rate necessary to reach a certain power output and hence the specific heat flux is reduced. However, this approach simplifies the highly complex conjugate heat transfer effects and should be fine-tuned iteratively. Consulting two prior publications on microgas turbine heat transfer [17,57] as well as looking at the preliminary conjugate heat transfer results, values of heat flux ratios r_{qc} and r_{qt} are estimated as 0.3.

In each incremental step, the next temperature is calculated according to the combined enthalpy change

$$T_{i+1} = T_i + \frac{\delta h_{\text{dia},i}}{c_p(T_i)} \tag{C9}$$

To calculate the work added or extracted during the pressure change, the incremental steps of compression or expansion are added up

$$w_{t/c} = \sum_{i=1}^{N} \delta w_{c/t} \tag{C10}$$

The specific work output and electric efficiency can then be found from

$$w_{\text{el}} = (w_t \cdot (1 + FAR) - w_c) \cdot \eta_m \cdot \eta_{\text{el}} \tag{C11}$$

$$\eta_{\text{el}} = \frac{w_{\text{el}}}{q_{\text{fuel}}} \tag{C12}$$

Iterative calculation of the cycle is conducted to provide sufficient convergence of combustion heat input and resulting turbine fuel ratio.

Appendix D: Analytic Calculation of Generator Dimensions

The review of previous efforts showed that rotordynamic instability is a major hurdle toward successful UMGT operation. As the generator dimensions have a significant impact on mode

Table 9 Generator model input

Input parameters	Values	Input parameters	Values
Operating speed	500,000 RPM	Air gap + sleeve thickness	1 mm
Target efficiency	90–99%	Coil filling factor	0.6
Shaft diameter	4 mm	Stator iron saturation	0.1–0.765 T
Generator diameter	20–30 mm	Generator back electromotive force	18 V
Phase angle β	0.2–0.5	Maximum current density	10 A/mm^2

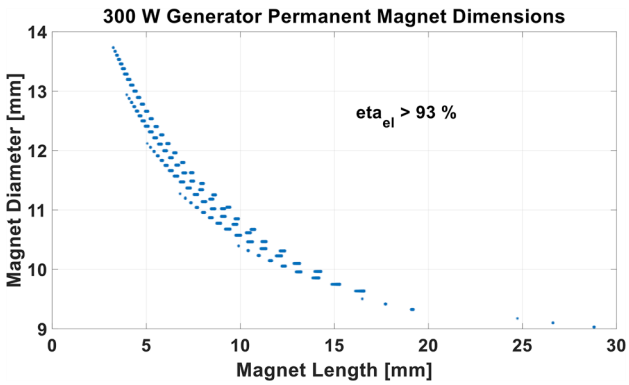

Fig. 17 Generator analytic model results

frequencies, an analytic sizing of the high speed generator is implemented based on design guidelines for a slotless brushless DC motor [42]. To find an optimum generator configuration, the outer motor radius, electric efficiency, phase angle, and field amplitude of the model are varied within reasonable ranges, summarized in Table 9. To exclude invalid designs, a maximum current density is defined and compared with the wire cross section and the resulting current. The inner diameter of the hollow cylinder magnet is limited by the bearing inner diameter (4 mm). The stator magnet made of Sm_2Co_{17} is implemented in the model with corresponding material properties.

Figure 17 shows the permanent magnet external dimensions for valid generators with an output of 300 W and efficiency of above 93%. To address rotordynamic stability analysis, a simplified engine model is designed from the geometrical information of meanline turbine and compressor design as well as the generator permanent magnet. This way, the system-level interdependency between thermodynamic cycle, turbomachinery design, and rotordynamics is established.

Appendix E: Thermodynamic Cycle Sensitivity Analysis

A sensitivity analysis is conducted to show the effect of different cycle parameters on electric efficiency. TIT and cycle pressure ratio alike have significant impact. Considering UMGT design, it is therefore most critical to not fall below the design values for these two parameters. This conclusion was also observed in previous efforts, where the design pressure ratio was not reached, or the TIT was reduced due to heat transfer effects.

The parameters used in the sensitivity study are summarized in Table 10, while the findings of the study are presented in Fig. 18. The data suggest that turbine and compressor heat flux factors do not create major impact on the cycle design point when compared to other parameters. Besides this, the combustor pressure drop is a driving parameter for cycle efficiency and the effect of a 3% change is more significant than changing the pressure ratio value by 0.3 or doubling compressor heat transfer. Therefore, reducing combustor pressure drop is paramount during UMGT development effort. In contrast to this, changing combustor efficiency by 2% does not cause a severe effect on cycle efficiency. Generator

Table 10 Sensitivity analysis parameters

	Lower limit	Reference	Upper limit
Turbine efficiency	69%	72%	75%
Compressor efficiency	65%	68%	71%
Turbine inlet temperature	1100 K	1200 K	1300 K
Pressure ratio	2.2	2.5	2.8
Turbine heat flux factor	0.4	0.3	0.2
Compressor heat flux factor	0.4	0.3	0.2
Combustor pressure drop	8%	5%	2%
Combustor efficiency	96%	98%	100%
Generator efficiency	90%	95%	100%
Mechanic efficiency	90%	95%	100%
Inlet pressure drop	1%	0.5%	0%
Outlet pressure drop	1%	0.5%	0%
Mechanic efficiency	90%	95%	100%

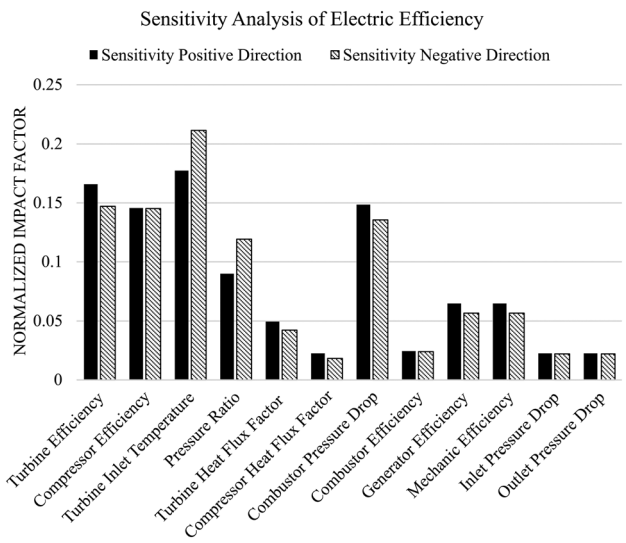

Fig. 18 Thermodynamic cycle sensitivity analysis

and mechanical efficiencies have direct impact on the shaft power and should therefore not be neglected. To summarize, the UMGT design guidelines stemming from case studies and sensitivity analysis are:

- To maximize turbine and compressor aerodynamic efficiency,
- To maximize TIT,
- To avoid excessive pressure ratio for low TITs due to reduced benefit,
- To reduce compressor and turbine performance deterioration by mitigating heat flux,
- To optimize combustor pressure drop.

Appendix F: Thermodynamic Cycle: Reference Scenario

In this section, the cycle analysis results are discussed to highlight a baseline scenario for component efficiency and heat transfer rates. The values for generator efficiency, mechanic efficiency, and pressure drops are kept constant as summarized in Fig. 19. The compressor polytropic efficiency is approximated as 68%, the turbine polytropic efficiency is 72% and the heat flux fraction of compressor and turbine is 0.3.

The effect of heat addition on cycle performance is considered according to previous equations. It can be seen that for low TITs, the optimum pressure ratio is rather low at a value of 3 for

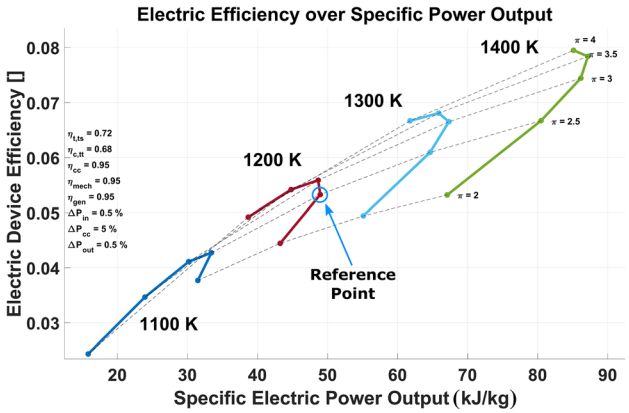

Fig. 19 Reference cycle evaluation considering diabatic effect

1100 K. This results from the diabatic processes and the low component efficiencies, which mitigate the resulting shaft power for higher pressure ratios. At a TIT of 1000 K, the optimum pressure ratio for highest efficiency is already 2.5. Further increase leads to reduced cycle efficiency and work output. This leads to the conclusion, that a direct connection between cycle analysis and component design is necessary during an early stage of UMGT development, in order to avoid issues faced by previous projects. There, high pressure ratio was set as an objective, leading to high speed bearing issues and preventing successful UMGT operation.

References

[1] BCC Research, 2018, "Drone Technology and Global Markets: Market Report Oct 2018," BCC Research, Wellesley, MA, Report No. IAS104B.

[2] Teal Group, 2020, "World Military Unmanned Aerial Systems: Market Profile & Forecast," Military UAV Market To Top $83B, Fairfax, VA, accessed Oct. 16, 2020, https://insideunmannedsystems.com/military-uav-market-to-top-83b/

[3] CompTIA, 2018, "The Drone Market: Insights from Customers and Providers," Research Report, The Drone Market: Insights from Customers and Providers, Downers Grove, IL, accessed Oct. 16, 2020, https://www.comptia.org/content/research/the-drone-market-insights-from-customers-and-providers

[4] Epstein, A. H., 2004, "Millimeter-Scale, Micro-Electro-Mechanical Systems Gas Turbine Engines," ASME J. Eng. Gas Turbines Power, **126**(2), pp. 205–226.

[5] Epstein, A. H., Jacobson, S. A., Protz, J. M., and Frechette, L. G., 2000, "Shirtbutton-Sized Gas Turbines: The Engineering Challenges of Micro High Speed Rotating Machinery," Proceedings of the Eighth International Symposium on Transport Phenomena and Dynamics of Rotating Machinery, Honolulu, Hawai, Mar. 26–30, pp. 26–30.

[6] Fréchette, L. G., Jacobson, S. A., Breuer, K. S., Ehrich, F. F., Ghodssi, R., Khanna, R., Wong, C. W., Zhang, X., Schmidt, M. A., and Epstein, A. H., 2000, *Demonstration of a Microfabricated High-Speed Turbine Supported on Gas Bearings*, Gas Turbine Laboratory and Microsystems Technology Laboratories Massachusetts Institute of Technology, Cambridge, UK.

[7] Orr, D. J., "Macro-Scale Investigation of High Speed Gas Bearings for MEMS Devices," Ph.D thesis, Massachusetts Institute of Technology, Cambridge, MA.

[8] Mehra, A., "Computational Investigation and Design of Low Reynolds Number Micro-Turbomachinery," Master thesis, Massachusetts Institute of Technology, Cambridge, MA.

[9] Isomura, K., Murayama, M., and Kawakubo, T., 2001, "Feasibility Study of a Gas Turbine at Micro Scale," ASME Paper No. 2001-GT-0101.

[10] Tanaka, S., Hikichi, K., Togo, S., Murayama, M., Hirose, Y., Sakurai, T., and Esashi, M., 2007, "World's Smallest Gas Turbine Establishing Brayton Cycle," Seventh International Workshop on Micro and Nanotechnology for Power Generation and Energy Conversion Applications (PowerMEMS 2007), Freiburg, Germany, Nov. 27–29, pp. 359–362.

[11] Tanaka, S., Isomura, K., Togo, S. I., and Esashi, M., 2004, "Turbo Test Rig With Hydroinertia Air Bearings for a Palmtop Gas Turbine," J. Micromech. Microeng., **14**(11), pp. 1449–1454.

[12] Park, C. H., Choi, S. K., and Ham, S. Y., 2011, "Design and Experiment of 400,000 rpm High Speed Rotor and Bearings for 500W Class Micro Gas Turbine Generator," 11th International Workshop on Micro and Nanotechnology for Power Generation and Energy Conversion Applications (PowerMEMS 2011), Seoul, Korea, Nov. 15–18.

[13] Park, J. S., Park, S., Kim, K. M., Choi, B. S., and Cho, H. H., 2013, "Effect of the Thermal Insulation on Generator and Micro Gas Turbine System," Energy, **59**, pp. 581–589.

[14] Seo, J., Lim, H. S., Park, J., Park, M. R., and Choi, B. S., 2017, "Development and Experimental Investigation of a 500-W Class Ultra-Micro Gas Turbine Power Generator," Energy, **124**, pp. 9–18.

[15] Seo, J. M., Park, J. Y., and Choi, B. S., 2013, "Start-Up and Self-Sustain Test of 500 W Ultra-Micro Gas Turbine Generator," J. Phys. Conf. Ser., **476**, p. 012060.

[16] Peirs, J., Waumans, T., Vleugels, P., Al-Bender, F., Stevens, T., Verstraete, T., Stevens, S., D'hulst, R., Verstraete, D., Fiorini, P., Van den Braembussche, R., Driesen, J., Puers, R., Hendrick, P., Baelmans, M., and Reynaerts, D., 2007, "Van Den Braembussche, R. "Micropower Generation With Microgasturbines: A Challenge," Proc. Inst. Mech. Eng., Part C, **221**(4), pp. 489–500.

[17] Verstraete, D., and Bowkett, C., 2015, "Impact of Heat Transfer on the Performance of Micro Gas Turbines," Appl. Energy, **138**, pp. 445–449.

[18] Peirs, J., Waumans, T., Al-Bender, F., and Reynaerts, D., 2010, "Experimental Verification of Compressor Performance for an Ultra-Microgasturbine," 10th International Workshop on Micro and Nanotechnology for Power Generation and Energy Conversion Applications (PowerMEMS 2010), Leuven, Belgium, Nov. 30–Dec. 3, pp. 99–102.

[19] Liu, H. C., Kang, S., Prinz, F. B., and Stampfl, J., 2002, "Fabrication of Ceramic Components for Micro Gas Turbine Engines," 26th Annual Conference on Composites, Advanced Ceramics, Materials, and Structures: B, The American Ceramic Society, Cocoa Beach, FL, Jan. 13–18, pp. 43–50.

[20] Johnston, J. P., Kang, S., Arima, T., Matsunaga, M., Tsuru, H., and Prinz, F. B., 2003, "Performance of a Micro-Scale Radial-Flow Compressor Impeller Made of Silicon Nitride," IGTC Tokyo, Tokyo, Japan, Nov. 2–7, Paper No. IGTC2003Tokyo OS-110.

[21] Kang, S., Johnston, J. P., Arima, T., Matsunaga, M., Tsuru, H., and Printz, F. B., 2004, "Microscale Radial-Flow Compressor Impeller Made of Silicon Nitride: Manufacturing and Performance," ASME J. Eng. Gas Turbines Power, **126**(2), pp. 358–365.

[22] Kang, S., "Fabrication of Functional Mesoscopic Ceramic Parts for Micro Gas Turbine Engines," Ph.D thesis, Stanford University, Stanford, CA.

[23] Dessornes, O., and Zwyssig, C., 2010, "Micro-Generator for Ultra Micro Gas Turbine," Power MEMS, Leuven, Belgium, Nov. 30–Dec. 3, pp. 195–198.

[24] Dessornes, O., Landais, S., Valle, R., Fourmaux, A., Burguburu, S., Zwyssig, C., and Kozanecki, Z., 2014, "Advances in the Development of a Microturbine Engine," ASME J. Eng. Gas Turbines Power, **136**(7), p. 71201.

[25] Whittfield, A., 1990, "The Preliminary Design of Radial Inflow Turbines," ASME J. Turbomach., **112**, pp. 50–57.

[26] Rodgers, C., and Geiser, R., 1987, "Performance of a High-Efficiency Radial/Axial Turbine," ASME J. Turbomach., **109**(2), pp. 151–154.

[27] Kyocera Corporation, 2019, "Material Properties of Ceramics," Kyocera Corporation, Kyoto, Japan, accessed Oct. 16, 2020, https://global.kyocera.com/prdct/fc/list/material/

[28] Special Metals Corporation, 2019, "Inconel Alloy 718," Special Metals Corporation, New Hartford, NY, accessed Oct. 16, 2020, www.specialmetals.com

[29] Special Metals Corporation, 2019, "Nimonic 115," Special Metals Corporation, New Hartford, NY, accessed Oct. 16, 2020, www.specialmetals.com

[30] High Temp Metals, 2015, "Rene 41 Technical Data," High Temp Metals, Sylmar, CA, accessed Oct. 16, 2020, https://www.hightempmetals.com/techdata/hitempRene41data.php

[31] Lithoz GmbH, 2019, "LCM—Technology," Lithoz GmbH, Vienna, Austria, accessed Oct. 2020, http://www.lithoz.com/en/additive-manufacturing/lcm-technology

[32] International Syalons, 2019, "3D-Printed Silicon Nitride," International Syalons, Wallsend, UK, accessed Oct. 16, 2020, https://www.syalons.com/2016/09/26/3d-printed-silicon-nitride/

[33] McLEAN, A. F., 1970, "The Application of Ceramics to the Small Gas Turbine," ASME Paper No. 70-GT-105.

[34] Kunz, W., Abel, J., Moritz, T., and Stockmann, J., 2016, "High-Performance Ceramics for Gas Turbines—From Materials to Components," Fraunhofer IKTS, Hermsdorf, Germany, Reprot No. IKTS Annual Report 2015/2016, pp. 26–27.

[35] Chevalier, J., Gremillard, L., and Deville, S., 2007, "Low-Temperature Degradation of Zirconia and Implications for Biomedical Implants," Annu. Rev. Mater. Res., **37**(1), pp. 1–32.

[36] Panda, P. K., Kannan, T. S., Dubois, J., Olagnon, C., and Fantozzi, G., 2002, "Thermal Shock and Thermal Fatigue Study of Alumina," J. Eur. Ceram. Soc., **22**(13), pp. 2187–2196.

[37] Wang, X., Gong, X., and Chou, K., 2017, "Review on Powder-Bed Laser Additive Manufacturing of Inconel 718 Parts," Proc. Inst. Mech. Eng., Part B, **231**(11), pp. 1890–1903.

[38] EOS GmbH—Electro Optical Systems, 2014, "EOS NickelAlloy IN718 Material Data Sheet," EOS GmbH—Electro Optical Systems, Krailling, Germany, accessed Oct. 16, 2020, https://www.rapidmade.com/inconel-718-nickel-alloy-direct-metal-laser-sintering-dmls-slm-3d-printing-data-sheet

[39] 3D Micromac AG, 2019, "3D-Printing Using Micro Laser Sintering," 3D-Printing Using Micro Laser Sintering, Chemnitz, Germany, accessed Oct. 16, 2020, https://3d-micromac.com/laser-micromachining/applications/3d-printing/

[40] Steinbach, A. G., 2020, "Design Guide," Design Guide, Steinbach AG, Detmold, Germany, accessed Oct. 16, 2020, https://www.steinbach-ag.de/en/technical-ceramics/know-how/design-guide.html

[41] Diegel, O., Nordin, A., and Motte, D., 2019, *A Practical Guide to Design for Additive Manufacturing*, Springer, Singapore.

[42] Markovic, M., and Perriard, Y., 2006, "Simplified Design Methodology for a Slotless Brushless DC Motor," IEEE Trans. Magn., **42**(12), pp. 3842–3846.

[43] Arroyo, A., McLorn, M., Fabian, M., White, M., and Sayma, A. I., 2016, "Rotor-Dynamics of Different Shaft Configurations for a 6 kW Micro Gas Turbine for Concentrated Solar Power," ASME Paper No. GT2016-56479.

[44] Marin, M. A., 2012, "Rotor Dynamics of Overhung Rotors: Hysteretic Dynamic Behavior," ASME Paper No. GT2012-68285.
[45] Hearn, E. J., 1997, *Mechanics of Materials 2: The Mechanics of Elastic and Plastic Deformation of Solids and Structural Materials*, Elsevier, Amsterdam, The Netherlands.
[46] Zwyssig, J., and Kolar, J. W., 2005, "Design of a 100 W, 500000 Rpm Permanent-Magnet Generator for Mesoscale Gas Turbines," 40th IAS Annual Meeting, Conference Record of the 2005 Industry Applications Conference, Kowloon, Hong Kong, Oct. 2–6, pp. 253–260.
[47] Mohamad, A. A., 2005, "Combustion in Porous Media: Fundamentals and Applications," Transport Phenomena in Porous Media III, Elsevier, Amsterdam, The Netherlands, pp. 287–304.
[48] Guidez, J., Roux, P., Poirson, N., Jourdanneau, E., Orain, M., and Grisch, F., 2009, "Investigation of Combustion in Miniaturised Combustor for Application to Micro Gas Turbines," Prog. Propul. Phys., **1**, pp. 469–480
[49] Sadasivuni, V., and Agrawal, A. K., 2009, "A Novel Meso-Scale Combustion System for Operation With Liquid Fuels," Proc. Combust. Inst., **32**(2), pp. 3155–3162.
[50] Turkeli-Ramadan, Z., Sharma, R. N., and Raine, R. R., 2014, "Clean Flat Flame Combustor for Ultra Micro Gas Turbine," Proceedings of 19th Australasian Fluid Mechanics Conference, Melbourne, Australia, Dec. 8–11, Paper No. 193.
[51] Tseng, C., and Howell, J. R., 1996, "Combustion of Liquid Fuels in a Porous Radiant Burner," Combust. Sci. Technol., **112**(1), pp. 141–161.
[52] Kaplan, M., and Hall, M. J., 1995, "The Combustion of Liquid Fuels Within a Porous Media Radiant Burner," Exp. Therm. Fluid Sci., **11**(1), pp. 13–20.
[53] Rusch, D., and Casey, M., 2013, "The Design Space Boundaries for High Flow Capacity Centrifugal Compressors," ASME J. Turbomach., **135**(3), p. 031035.
[54] Casey, M. V., 2014, "Centrifugal Compressor Design," Israeli Symposium on Turbomachinery and Jet Engines and Gas Turbines, Haifa, Israel, Nov. 2, Paper No. A4.
[55] Chinnaswamy, S., 2015, "The Impact of Surface Roughness on Transonic Compressor Performance," Master's thesis, Department of Applied Mechanics, Chalmers University of Technology, Göteborg, Sweden, pp. 1652–8557.
[56] Adams, T., Grant, C., and Watson, H., 2012, "A Simple Algorithm to Relate Measured Surface Roughness to Equivalent Sand-Grain Roughness," Int. J. Mech. Eng. Mechatronics, **1**(2), pp. 66–71.
[57] Verstraete, T., Alsalihi, Z., and van den Braembussche, R. A., 2007, "Numerical Study of the Heat Transfer in Micro Gas Turbines," ASME J. Turbomach., **129**(4), pp. 835–841.
[58] Munro, R., 2005, "Evaluated Material Properties for a Sintered Alpha-Alumina," J. Am. Ceram. Soc., **80**(8), pp. 1919–1928.
[59] Kondoh, J., Shiota, H., Kawachi, K., and Nakatani, T., 2004, "Yttria Concentration Dependence of Tensile Strength in Yttria-Stabilized Zirconia," J. Alloys Compd., **365**(1–2), pp. 253–258.
[60] Evans, A. G., and Wiederhorn, S. M., 1974, "Crack Propagation and Failure Prediction in Silicon Nitride at Elevated Temperatures," J. Mater. Sci., **9**(2), pp. 270–278.
[61] Achtelik, M., Doth, K., Gurdan, D., and Stumpf, J., 2012, "Design of a multi rotor MAV With Regard to Efficiency, Dynamics and Redundancy," AIAA Paper No. 2012-4779.
[62] Luomi, J., Zwyssig, C., Looser, A., and Kolar, J. W., 2009, "Efficiency Optimization of a 100-W 500 000-r/Min Permanent-Magnet Machine Including Air-Friction Losses," IEEE Trans. Ind. Appl., **45**(4), pp. 1368–1377.
[63] Zwyssig, 2006, "Analytical and Experimental Investigation of a Low Torque, Ultra-High Speed Drive System," Conference Record of the IEEE Industry Applications Conference Forty-First IAS Annual Meeting No. 3, Tampa, FL, Oct. 8–12, pp. 1507–1513.
[64] Zwyssig, 2006, "Power Electronics Interface for a 100 W, 500000 rpm Gas Turbine Portable Power Unit," Twenty-First Annual IEEE Applied Power Electronics Conference and Exposition, Dallas, TX, Mar. 19–23, pp. 283–289.
[65] McBride, B. J., 2002, *NASA Glenn Coefficients for Calculating Thermodynamic Properties of Individual Species*, National Aeronautics and Space Administration, John H. Glenn Research Center at Lewis Field, Cleveland, OH.
[66] Visser, W. P. J., Shakariyants, S. A., and Oostveen, M., 2011, "Development of a 3 kW Microturbine for CHP Applications," ASME J. Eng. Gas Turbines Power, **133**(4), p. 042301.
[67] Visser, W. P., and Broomhead, M. J., 2000, "GSP, a Generic Object-Oriented Gas Turbine Simulation Environment," ASME Paper No. 2000-GT-0002.
[68] Kurzke, J., 2007, *GasTurb 11: Design and Off-Design Performance of Gas Turbines*, GasTurb GmbH, Aachen, Germany.
[69] Casey, M. V., and Fesich, T. M., 2010, "The Efficiency of Turbocharger Compressors With Diabatic Flows," ASME J. Eng. Gas Turbines Power, **132**(7), p. 72302.
[70] Nagashima, T., Okamoto, K., and Ribaud, Y., 2005, "Cycles and Thermal System Integration Issues of Ultra-Micro Gas Turbines, (Lecture Series on Micro Gas Turbines)," NATO Research and Technology Organisation, Neuilly-sur-Seine, France, Standard No. RTO-EN-AVT-131.
[71] Shaaban, S., and Seume, J., 2012, "Impact of Turbocharger Non-Adiabatic Operation on Engine Volumetric Efficiency and Turbo Lag," Int. J. Rotating Mach., **2012**, pp. 1–1.